Rotation Control, Interlocking, and Self-Positioning of Active Cogwheels

Quentin Martinet, Antoine Aubret, and Jeremie Palacci*

Gears and cogwheels are elemental components of machines. They restrain degrees of freedom and channel power into a specified motion. Building and powering small-scale cogwheels are key steps toward feasible micro and nanomachinery. Assembly, energy injection, and control are, however, a challenge at the microscale. In contrast with passive gears, whose function is to transmit torques from one to another, interlocking and untethered active gears have the potential to unveil dynamics and functions untapped by externally driven mechanisms. Here, it is shown the assembly and control of a family of self-spinning cogwheels with varying teeth numbers and study the interlocking of multiple cogwheels. The teeth are formed by colloidal microswimmers that power the structure. The cogwheels are autonomous and active, showing persistent rotation. Leveraging the angular momentum of optical vortices, we control the direction of rotation of the cogwheels. The pairs of interlocking and active cogwheels that roll over each other in a random walk and have curvature-dependent mobility are studied. This behavior is leveraged to self-position parts and program microbots, demonstrating the ability to pick up, direct, and release a load. The work constitutes a step toward autonomous machinery with external control as well as (re)programmable microbots and matter.

1. Introduction

Biological nanomachines enable life by powering dynamic processes across scales:[1] molecular motors organize chromosomes,[2] assist cell division, and drive muscular contraction.[3] Emulating comparable complex behavior in synthetic systems requires the engineering of micromachines that rival their biological counterparts. The challenges to the task are manifold: 1) adequate small-scale fabrication and self-assembly, 2) tools of control and computation in a noisy environment, and 3) power generation at the micro and nanoscale. Achieving this requires the development of novel strategies, marrying tools of basic science with modern robotics.[4,5] The field of active colloids—microscale particles that transduce energy at a small scale—is uniquely suited to overcome the challenges and lay the groundwork for autonomous microbots of untapped complexity and versatility.[6–8] First, progress in colloidal science enables the bespoke design of microscale building blocks with programmable interactions[9–13] for self-assembly.[14–18] Second, energy harvesting by the active colloids can power motility and elementary computation. Colloidal microswimmers orient themselves autonomously in flows,[19,20] navigate noisy and unexplored environments using machine learning strategies[21] or communicate via clouds of chemicals.[22,23] Recent proofs of concept have notably stressed the relevance of the approach for biomedical applications:[24–26] micropropellers penetrate the vitreous body of the eye,[27] multifunctional rollers deliver cargos in physiological blood flow[28] and enzymatic nanomotors travel to the bladder in vivo.[29] The progress remains however primarily limited to single active agents as machines, lacking coordination between parts. The dynamics of adaptative mechanisms important for complex machinery, such as the interlocking of untethered cogwheels, is largely unexplored. Active cogwheels can be obtained using microfabricated devices powered by active colloids or bacteria,[30–32] momentum transfer from light,[33] light-driven dielectrophoretic forces,[34,35] or thermocapillary effects.[36] They, moreover, constitute large ($> 30\,\mu m$) and monolithic structures, whose direction of rotation is encoded in a rigid template. However, the aforementioned works did not study the dynamics of interlocking pairs nor address their potential in microrobotics.

In contrast, we recently proposed a novel approach that uses templates of optical traps to program metamachines, or machines made of machines, from active colloids. Our approach harnesses the interplay between the optical forces exerted on an active colloid and its self-propulsion. It does not require light-activated particles and applies, in principle, to a broad variety of colloidal microswimmers, e.g., Janus Pt particles, and fuels.[37]

Q. Martinet, A. Aubret,[+] J. Palacci
Department of Physics
University of California San Diego
92093 La Jolla, USA
E-mail: jeremie.palacci@ist.ac.at

Q. Martinet, J. Palacci
IST Austria
Am Campus 1, 3400 Klosterneuburg, Austria

The ORCID identification number(s) for the author(s) of this article can be found under https://doi.org/10.1002/aisy.202200129.

[+]Present address: Univ. Bordeaux, CNRS, LOMA, UMR 5798, F-33405 Talence, France

For the present work, we leverage this method to assemble a family of autonomous cogwheels with a varying number of teeth. We propose a novel optical development that harnesses the angular momentum of optical vortices to set the direction of rotation of cogwheels. We study the dynamics of the cogwheels and the behavior of interlocking cogwheels in contact. In contrast with passive cogwheels, which function is to transmit torques, our active cogwheels are untethered and mobile. They roll over each other and exhibit a diffusive behavior when interlocked, with a mobility that depends on the curvature. This behavior enables elementary onboard computation of the curvature of a structure, which can be used to assemble machines by autonomously positioning parts. The work highlights untapped opportunities for architectures and microbots made from active components.

2. Results and Discussion

2.1. Assembly of a Family of Active Cogwheels

A family of self-spinning cogwheels is built following an algorithm for the assembly of machines from self-propelled colloids that we recently unveiled.[37] In brief, a colloidal bead is optically trapped and decorated with N peripheral optical traps, N being the number of teeth for the cogwheel (**Figure 1**A). Active heterodimers travel along the substrate and are captured when crossing the optical traps. The trapping originates from the interplay between alignment by repulsive scattering forces and propulsion,

as previously reported.[37] As a result, we can assemble cogwheels made of a central sphere surrounded by N peripheral heterodimers: the teeth of the cogwheel. The optical traps are subsequently removed and the cogwheel spins autonomously. The procedure is repeated with different N to form a collection of cogwheels with varying teeth numbers (Figure 1B, Movie S1, Supporting Information). Practically, we use identical active heterodimers of radii d and vary the radius of the central particle to control the number of teeth N of the cogwheel. The experimental results are unaffected by the use of different materials for the central bead: silica, polystyrene, or TPM polymer. The central bead constitutes a confining boundary along which active colloids travel, effectively leading to the rotation of the cogwheel. Repeating the procedure for central beads of increasing radii, we find that stable cogwheels correspond to active heterodimers packed on the periphery of the central sphere, i.e., $2\pi R = 2Nd$. Slight deviations from compact packing yield unstable structures that disassemble (Figure 1C). From time-lapse videos, we obtain the average rotation rate $\overline{\Omega}_N$ for self-spinning cogwheels with $N = 6$–13 (Figure 1D) and orientation θ_N of the heterodimers forming the teeth of the cogwheel (Figure 1E). Remarkably, the mean orientation $\overline{\theta}_N$ follows $\cos\overline{\theta}_N \propto 1/R$ (Equation (1)) (Figure 1F), highlighting a coupling between the orientation of the heterodimers of the cogwheel and curvature. A quantitative description of the scaling requires detailed modeling of hydrodynamics and phoretic interactions in these multi-body systems and is beyond the scope of this article. We, however,
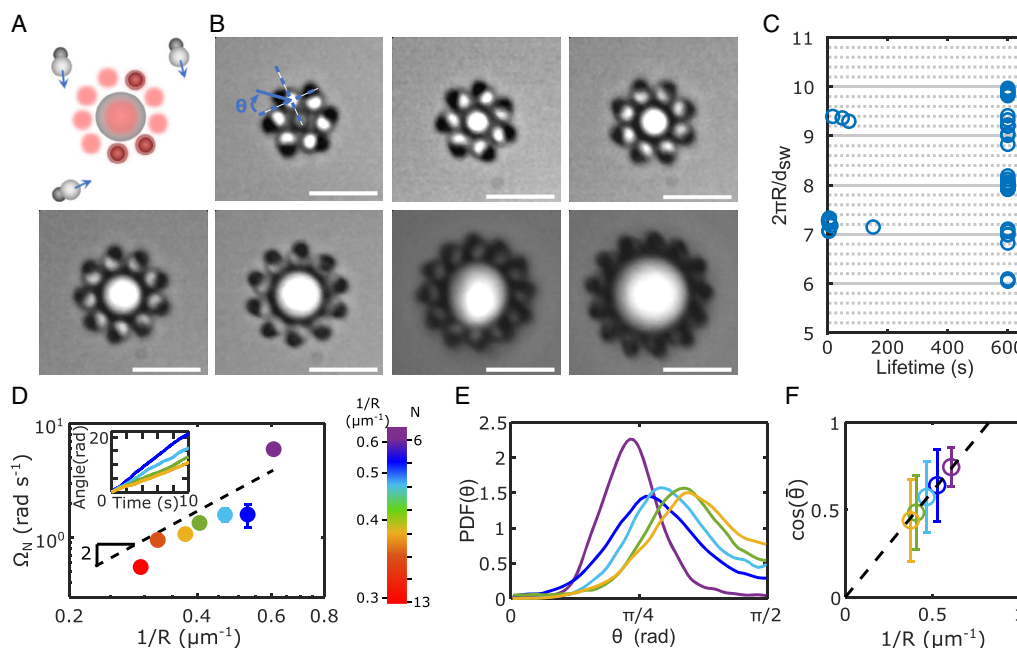

Figure 1. Family of Spinning Cogwheels. A) Formation of a cogwheel using templates of optical traps (in red). A bead is trapped in a center trap and decorated with optical traps at the periphery, then occupied by active heterodimers. Following their occupancy, the traps are removed, and the structure starts spinning, forming an autonomous cogwheel. B) Family of Cogwheels for $N = 6$ to $N = 13$. Scale bar is 5 μm. C) Cogwheels whose perimeter is an integer of the heterodimer's diameter d are stable and are observed over 600 s, other structures quickly collapse. D-inset) Temporal evolution of the rotation angle of the cogwheels showing persistent rotation. D) Amplitude of the Angular Velocity Ω_N of the rotation of the cogwheels, for different numbers of teeth $N = 6$–13 (see the adjacent color bar for correspondence between symbol color and N). Comparison of the experimental data with predicted scaling $\Omega_N \propto 1/R^2$ (dashed line, see main text). E) Probability distribution function (PDF) of the orientation θ of the heterodimers of the cogwheels for variable teeth number N. F) The mean value of the distribution $\overline{\theta}$ obtained from the PDF scales as $\cos\overline{\theta} \propto 1/R$.

use this empirical relationship to relate the rotation rate of the cogwheels with their curvature. As the rotation of the cogwheel results from the translational velocity V_0 of the active heterodimers, we expect $R\overline{\Omega}_N \propto V_0 \cos\overline{\theta}_N$, leading to $\Omega_N \propto 1/R^2$ (Equation (2)), in reasonable agreement with experimental data (Figure 1D).

2.2. Rotation Control by Optical Vortices

At this point, we have demonstrated the assembly of a family of spinning cogwheels with tunable number of gears. After release of the template, the active heterodimers that form the teeth momentarily fluctuate before the cogwheel starts spinning. The direction of rotation is random, resulting from a spontaneous symmetry-breaking. Fluctuations in the orientation of the heterodimers can stop the rotation, before reversing or not the direction of rotation (Movie S2, Supporting Information). The random reversal of directions is more frequently observed for gears with $N > 8$, which exhibit larger fluctuations of orientations (Figure 1E). This increase of fluctuations notably originates from lower rotation speeds for cogwheels with larger N, in line with experimental results that show a stabilizing effect of hydrodynamics in the orientation of the heterodimers.[37] Our aim is now to control the direction of rotation and to this end, we leverage the versatility of light to manipulate matter at a small scale. We use an optical vortex: a helical beam that displays a circular motion with an amount of orbital angular momentum $\ell\hbar$ per photon, where ℓ is an integer number and order of the vortex and $\hbar$ is the Planck constant.[38,39] The optical vortex induces a torque on a cogwheel (**Figure 2**A), transferring orbital angular momentum to the hematite of the heterodimer.[37] We quantify this torque by measuring the rotation rate of a spinning cogwheel ($N = 6$) illuminated by an optical vortex of opposite chirality and variable amplitude. Increasing the power of the optical vortex does not affect the geometric arrangement of the cogwheel, and results in a linear reduction of the angular speed of the cogwheel, as expected from the transfer of angular momentum by the photons (Figure 2B). The cogwheels notably stalls, $\Omega_6 = 0$ rad s^{-1}, for an incident power of $P\sim 5$ mW, which results in an optical torque exerted by the vortex, $T_6^* = 6\alpha_\ell Q_h P/c \sim 6$ pN μm, where the six prefactor accounts for the angular momentum transfer to $N = 6$ heterodimers, α_ℓ is a geometric factor accounting for the distribution of light for an optical vortex of order ℓ, Q_h is the absorption cross-section of the heterodimer and c is the speed of light (see Supporting Information for details on the estimate of Q_h, extension of the optical vortex as a function of ℓ and its derivation). This value for the optical torque to stop the rotation is in reasonable agreement with the estimate of the mechanical torque $T\sim 8\pi\eta R^3\Omega_6 \sim 3.5$ pN μm for a cogwheel of radius $R = 3$ μm rotating at $\Omega_6 \sim 5$ rads^{-1} in a fluid of viscosity $\eta = 10^{-3}$ Pas. We leverage this optical torque to set the orientation of the cogwheels and control their direction of rotation. Following the assembly and immobilization of a cogwheel by optical traps (Figure 2C), a short application (≈ 100 ms) of an optical vortex controls the direction of rotation, which persists after the removal of the optical vortex (Figure 2C). The procedure is repeated using optical vortices of opposite helicity to reverse the direction of rotation, exhibiting remarkable reproducibility on the rotation rate over
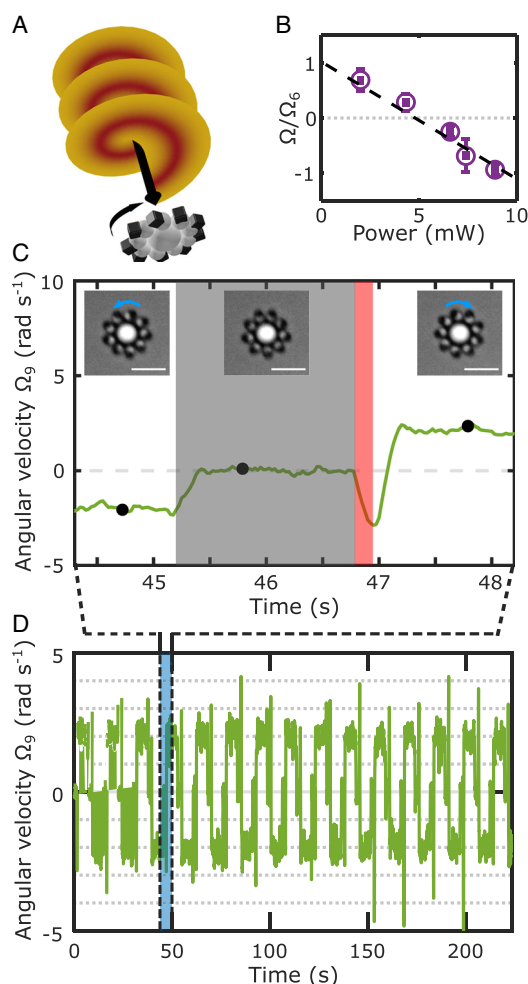
Figure 2. Rotation control of Cogwheels using Optical Vortices. A) 3D-rendering of a helical beam, i.e., an optical vortex, and optical momentum transfer to a cogwheel (in gray). B) Normalized angular velocity of a cogwheel, with $N = 6$, subject to the optical torque from a superimposed optical vortex of opposite chirality for varying power. The angular velocity of the cogwheel linearly reduces with incident light power, confirming the opposite torque imposed by the optical vortex. The angular velocity vanishes for $P\sim 5$ mW, when the optical torque of the vortex balances propulsion (see main text). C) Experimental procedure leading to the control of rotation of the cogwheels using optical vortices and measurement of the rotation velocity of a cogwheel, with $N = 9$ (green trace). The cogwheel is initially spinning counter-clockwise. It is shortly immobilized (≈ 1 s) by a template of optical traps (gray area). The traps are removed and an optical vortex is applied briefly (≈ 100 ms, red area), applying a torque that reorients the teeth and sets the rotation of the cogwheel. The cogwheel spins clockwise. In the inset, bright field images of the cogwheel corresponding to the black dot on the timeline. Scale bar is 5 μm. D) The procedure is repeated to control the direction of rotation over 15 cycles of reversal, exhibiting remarkable reproducibility of the rotation velocity. The shaded area corresponds to the timeline shown in (C).

multiple cycles of direction reversal (Figure 2D, Movie S3, Supporting Information). The procedure is similarly extended to cogwheels with different numbers of teeth and radii by adapting the order of the beam, i.e., radius of the optical vortex, to the

2200129 (3 of 8)

size of the cogwheel (Figure S4, Supporting Information). Our approach notably differs from previous works that achieved control of rotation of structures using optical[40] and optoelectronic[34] tweezers, magnetic actuators in a rotating magnetic field,[41] or photoactive liquid-crystal elastomers.[42] Those works use monolithic and passive structures and the aforementioned techniques effectively force the rotation. In contrast, we use optical vortices to orient a structure that autonomously spins. The orientation is controlled externally by the brief application of the optical vortex but is stable after the removal of the optical vortex. As a result, our approach does not require the permanent application of an external torque to achieve persistent rotation.

2.3. Dynamics of Interlocked Cogwheels

Two cogwheels interact at a long distance via phoresis, leading to synchronization mediated by clouds of chemicals. The description of the synchronization can be found in,[43,44] with the notable predictions that the radial component of the interaction decays rapidly with distance, $\propto 1/r^{N+2}$, where r is the center to center distance between two cogwheels and N is the teeth number. Distant synchronization notably requires trapping the center of the cogwheels to prevent them from drifting apart due to phoretic repulsion.[43,44] We instead turn to the study of the interlocking behavior of untethered pairs of cogwheels in contact.

We consider a cogwheel with a fixed number of teeth, $N_1 = 8$, in contact with a second cogwheel, for which N_2 varies between $N_2 = 6$ and $N_2 = \infty$, the flat interface of a rod-like structure. Using optical traps to manipulate the position of the center of the structures, the cogwheels are set in contact and released from the traps. Heterodimers near contact reorient vertically, resulting in an attractive interaction from hydrodynamic pumping:[37,45,46] gears of the two cogwheels interlock (**Figure 3**A. The structure is stable and interlocking cogwheels remain in contact over periods
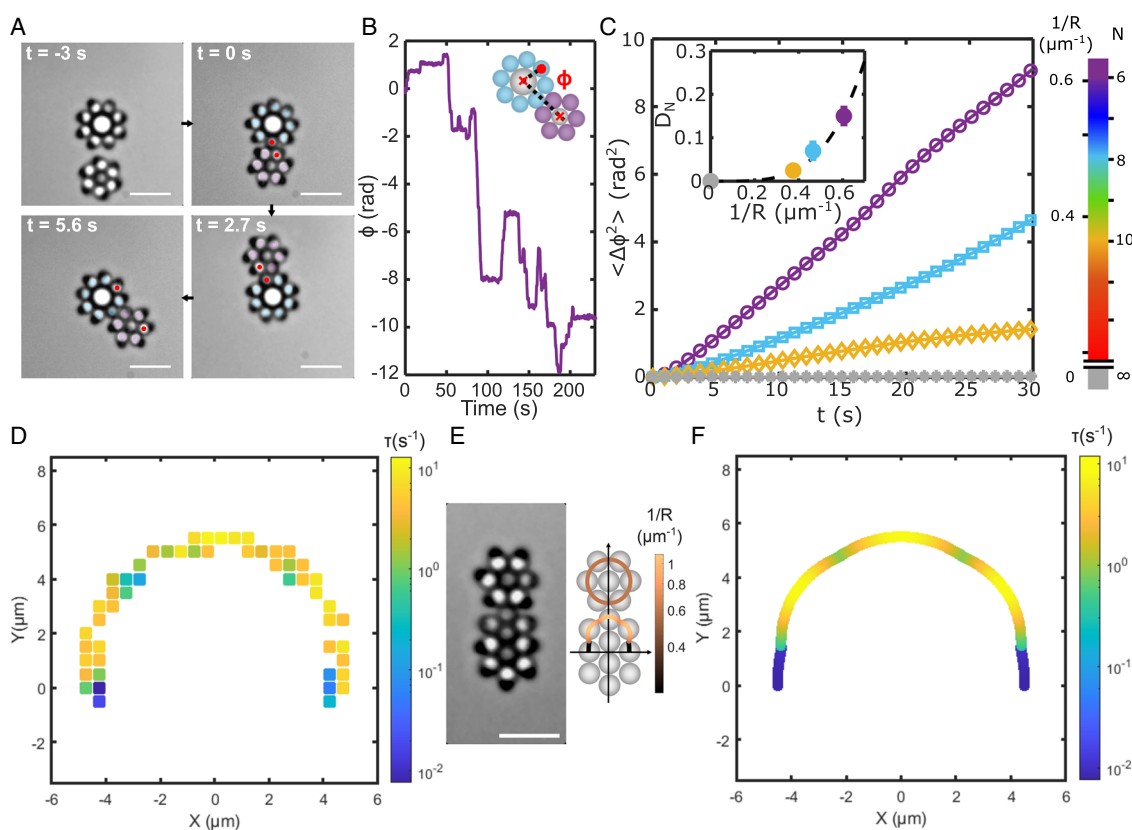
Figure 3. Interlocking cogwheels in contact. A) Timelapse of interlocking cogwheels. After assembly, they are put in contact using optical traps and then released at $t = 0$ s. They interlock and remain in contact, rolling over each other. The red dot is tethered to a teeth and a visual guide to see the rolling. B-inset) Definition of the angle Φ measuring the relative position of the cogwheels. B) Time evolution of $\Phi(t)$ measured experimentally, showing the rolling of the cogwheels, as well as the reversal of directions of rotation. C) Time evolution of the mean squared angular displacement (MSAD) $\Delta\Phi^2(t)$ for a central cogwheel, with $N = 8$, interlocked with cogwheel of increasing curvature. The MSAD increases linearly with time, indicative of an angular random walk with a curvature-dependent mobility D_N. C-inset) Measurement of diffusivity D_N from MSAD and comparison to the predicted scaling $D \propto 1/R^4$ (dashed line, see main text). D–F) Dynamics of a cogwheel interlocked with a structure of variable curvature. D) Experimental measurement of $1/\tau$ along the structure of variable curvature, where τ is the time spent by the cogwheel at position (X, Y). E-left) Bright-field image of a cogwheel interlocked with a structure of variable curvature. Scale bar is 5 μm. E-right) Simplified model of the structure in (E-left) and curvature value (color bar). (F) Numerical prediction of $1/\tau$, where τ is the time spent by the cogwheel at the position (X, Y), using the measured relationship $D \propto 1/R^4$ on the simplified structure depicted in (E-right). We observe a good agreement with the experimental value. Experiment and numerical results notably exhibit a stable configuration on areas of vanishing curvature.

**ADVANCED
SCIENCE NEWS**

www.advancedsciencenews.com

**ADVANCED
INTELLIGENT
SYSTEMS**
Open Access

www.advintellsyst.com

of time > 600 s. Cogwheels spin and roll over each other, akin to untethered macroscopic cogwheels with interpenetrating gears. The dynamics is, however, subject to fluctuations: the rotation of the cogwheels can stop and cogwheels can reverse directions (Figure 3B, Movie S4, Supporting Information). To quantify the dynamics, we quantify the motion of pairs of gears and represent the time evolution of the mean squared angular displacement (MSAD) $\Delta\phi^2(t)$ for the angle ϕ (Figure 3B-inset). We measure $\Delta\phi^2(t) = 2D_N t$ (Figure 3C), indicative of cogwheels rolling over each other in a random walk with a diffusivity D_N that depends on the number of teeth N, modified by changing the radius of the central sphere of the cogwheel. The mobility D_N is rapidly decreasing with the number of teeth of the cogwheel or equivalently its curvature, $1/R_N$, and vanishes on a flat interface, $R = \infty$ (Figure 3C-inset). For a cogwheel with a rotation rate Ω_N that is interlocked with an adjacent surface and can reverse direction randomly, we expect to observe a linear MSAD with diffusivity $D_N \propto \Omega_N^2$. Using [Equation (2)] prescribing $\Omega_N \propto 1/R^2$, we predict a curvature-dependent mobility $D_N \propto 1/R^4$, in agreement with our experimental data (Figure 3C-inset).

3. Discussion

Our results show that a cogwheel interlocked with a structure with variable curvature constitutes a stable pair with a dynamical structure. To test this prediction, we study the dynamics of a cogwheel, with $N = 8$, put in contact with a structure of variable curvature (Figure 3E). The cogwheel travels along the structure before fixing its position where curvature vanishes. We repeat the experiment to explore configurations and represent the escape rate $1/\tau$, which is the inverse of the time $\tau(X, Y)$ spent at a given position (X, Y) (Figure 3D). We successfully reproduce the observed dynamics using a simple model of a random walker with mobility $D \propto 1/R^4$ on a simplified model of a structure with

variable curvature (Figure S3E,F, Supporting Information). The experiment and model notably predict the self-positioning of active cogwheels on the flat edge of structures. We leverage this effect to program different microbots from cogwheels and shapes (**Figure 4**A, Movie S5, Supporting Information). In the first experiment, we assemble two shapes with the variable curvature characterized above (Figure 3D–F) and set their flat edge in contact with a cogwheel as a third structure. The formed microbot exhibits a steady shape and does not reconfigure (Figure 4A-left panel). In contrast, when two cogwheels are put in contact with a third one, they roll until they meet and merge, resulting in a different microbot (Figure 4A). The reconfiguration is reproducible and reliable, with the parts of the microbots consistently repositioning to form the targeted microbot.

We finally highlight the potential relevance of the achieved microbots for manipulation on a small scale. We demonstrate their use to capture, displace and release a load comprised of a passive sphere (Figure 4B, Movie S6, Supporting Information). The load is first encapsulated by a layer of active heterodimers, using templates of optical traps, as discussed earlier. It isolates the load from its surroundings to assemble a cogwheel (Figure 4B). A structure with variable curvature is similarly assembled independently. The two structures are brought together and merged, leading to the formation of a microbot. The microbot is powered by the active heterodimers of the structure and exhibits translational velocity.[37] The structure reorients randomly from collisions with the solvent and fluctuations in the orientation of the heterodimers so that the direction of propulsion evolves with time. However, the rotational diffusion is slow, owing to the large dimension of the structure. External control of the direction of migration of the cargo is added by leveraging the phototactic behavior of the composing heterodimers under non-uniform illumination.[44] We use a gradient of blue light to direct the microbot, as shown by the propulsion along a persistent and constant direction
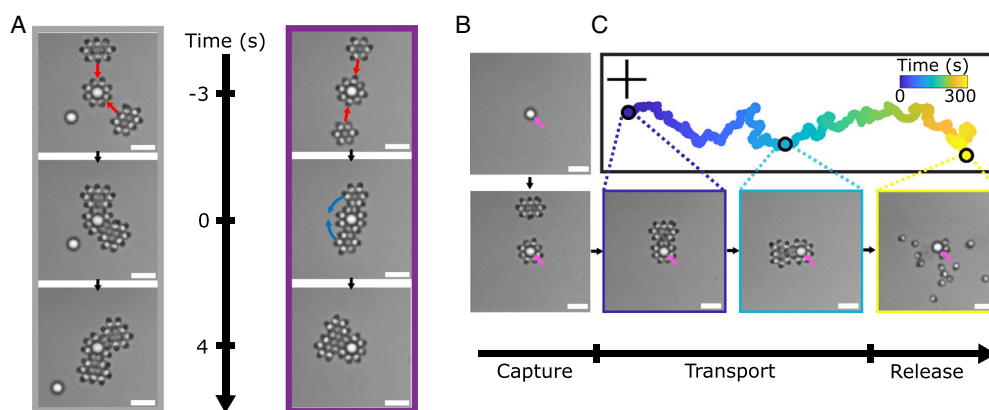
Figure 4. Reprogrammable Microbots and Cargo Transport. A) Self-positioning of structures. A central cogwheel, with $N = 8$, is interlocked with two structures with a flat edge (left) or two cogwheels, with $N = 6$ and constant curvature. A-left) It forms a stable structure, which shape does not change. A-right), the cogwheels roll over the central cogwheel and self-position to form a targeted microbot. B,C) Cargo Transport and Release. B) Timelapse bright field images. A passive cargo (pink arrow) is encapsulated and surrounded by active heterodimers to form a cogwheel. The cogwheel is merged to form a microbot with translational motion. The microbot navigates and the load is released on demand by simply turning off the activity of the swimmers. C) Trajectory of the microbot transporting the cargo and bright field images of the system at the time highlighted on the trajectory. The persistent migration of the cargo along a constant direction is controlled with a gradient of the (blue) light used to activate the heterodimers. It is used to direct the cargo. The cargo is delivered by turning off the activity, leading to the disassembly of the microbot and release of the cargo. Cross is a 20 μm scale bar.

**ADVANCED
SCIENCE NEWS**

www.advancedsciencenews.com

**ADVANCED
INTELLIGENT
SYSTEMS**

www.advintellsyst.com

(Figure 4C). The load is delivered on demand by turning off the activity of the active heterodimers so that the system returns to equilibrium. Particles composing the microbots become passive and diffuse away, and the microbot disassembles releasing its cargo (Figure 4B, Movie S6). Several strategies have been similarly proposed to manipulate cargos at the microscale using direct contact,[47,48] magnetic attractions,[49,50] electrostatic forces,[51,52] hydrodynamic flow,[53,54] or based on biohybrid microswimmers.[55,56] A recent computational study[57] even proposed to use the collaboration of self-propelled particles to trap and surround a cargo to navigate through a maze. Here, we devised a more complex microbot, using the load as a part and entirely directed by light. The direction of rotation is set by optical vortices, and the migration follows optical tracks formed by a light gradient with on-demand formation and release of microscopic cargos.

4. Conclusion

This work demonstrates the potential of active colloids to form autonomous machinery and mechanisms, with external control. Using self-positioning components shows a unique way of manufacturing machines, enviable at all scales, and particularly valuable at the microscale, where an accurate and robust assembly is challenged by noise. It highlights how modern robotics can benefit from fundamental advances in colloidal science and active matter and paves the way for reprogrammable matter.[58,59] The ability to direct the mechanism using external stimuli, such as light patterns, or concentration gradients to achieve cyclic transformations or programmable morphing of structures remains to be explored. Similarly, the communication between structures and coordinated movement between parts is a challenge on the path toward advanced types of machinery. It will be interesting to investigate the torque transmission from active cogwheels to passive gears. Active cogwheels that power passive microstructures have the potential for active microfluidics and robotics on a small scale.

5. Experimental Section

Optical Setup: The experiments were carried out on a custom-made optical setup, allowing for simultaneous uniform excitation of the microswimmers and optical patterns for trapping or optical vortices. The scheme of the optical setup is presented in (Figure S1, Supporting Information). The sample was observed with bright-field transmitted illumination (LED1). An LED was set up in the blue range (LED2, $\lambda = 425 - 500$ nm, Lumencor SOLA 6-LCR-SC) and uniformly illuminated the sample (illuminated area ~300×300 µm^2) to activate the swimmers by triggering the photocatalytic decomposition of H_2O_2 by the hematite (typical intensity of ≈ 1 µW µm^{-2}). A red continuous laser with near TEM00 mode ($\lambda = 639$ nm, Coherent, Genesis MX639-1000 STM, $M^2 < 1.1$) was added to the optical path. The linearly polarized beam was collimated, rotated with a $\lambda/2$ waveplate, and sent on the surface of a spatial light modulator (SLM, Holoeye -LETO Phase Only Spatial Light Modulator). The optical path followed a typical 4-f setup using two $f_1 = 400$ mm lenses, and the zero-order of the diffracted beam was filtered out with a diaphragm at an equal distance $d = f$ between the two lenses. Following, a hologram was formed at the back aperture of a high NA objective (Nikon apo-TIRF, $\times 100$, NA = 1.45) allowing for the creation of complex spatiotemporal optical patterns in the object

plane, at the bottom surface of the sample. The hologram was computed in real time using a computer software (Holoeye), with the phase patterns computed under MATLAB, and allows for the selective trapping and manipulation of individual swimmers. An electronic shutter (Thorlabs SHB1T) on the red optical path enables switching ON and OFF the laser traps. The sample was mounted on a manual micrometric stage (Nikon Ti-SR). Observation is performed through the same objective as for excitation, and the bright-field signal is reflected on a polarizing beam splitter and observed on two monochrome charged coupled devices (CCDs) with different resolutions (0.05 µm px^{-1} and 0.1 µm px^{-1}, respectively, Edmund Optics EO-1312M), with appropriate spectral filters. The optical vortex part was performed through phase modulation with a helicoidal phase profile $e^{i\ell\phi}$ (See Supporting Informaltion for more characterization of the optical vortex).

Image Acquisition and Analysis: All experiments were recorded on the CCD camera with 0.05 µm px^{-1} resolution, at a frame rate between 20 and 50 fps, and under bright field illumination. When necessary, tracking was performed separately for the hematite and TPM particles with a custom-made MATLAB routine. Error bars were obtained from standard deviations of experimental measurements.

Synthesis of Photocatalytic Hematite Cubes: The synthesis of hematite cubes followed the method described by Sugimoto.[60] We mix (100 mL, 2 M) FeCl$_3$ · 6H$_2$O, (90 mL, 6 M) NaOH, and (10 mL) water, in a 250 mL pyrex bottle and shake thoroughly. The bottle is placed in an oven at 100 °C for 3–4 days, until the hematite cubes reached the desired size. The hematite cubes of the gel were isolated by successive sedimentation and resuspension in deionized water (Milli-Q, resistivity 18.2 MΩ cm).

Synthesis of Active Heterodimers: Synthesis of heterodimer particles was performed by heterogeneous nucleation of trialkoxysilanes (oil precursor) on hematite particles as seeds. The synthesis procedure is adapted from,[61] with chemical modification to reinforce the stability of the heterodimer under light illumination. In particular, we make use of a hydrophobic copolymer hexadecyltrimethoxysilane (HTS) to chemically protect the bond between the hematite and polymer core against highly reactive hydroxyl radicals generated during H_2O_2 consumption. A beaker with (100 mL) of DI water was prepared, and mixed with (120 µL) of a 50% NH$_3$ solution, giving a pH ≈ 10.5, under mild magnetic stirring. ≈ 1 mL of an aqueous solution of hematite particles was added to get a slightly red-colored solution. Following, 100 µL of HTS was added, followed by (500 µL) of 3-(trimethoxysilyl)propyl methacrylate (TPM). The solution was covered and stirred for $\approx 2h$. During this time, the HTS and TPM hydrolyzed and condensed on the hematite particles, with strong wetting leading to their engulfment in the oil phase. After $\approx 2h$, the solution was turbid, as a result of the scattering of newly formed colloidal particles. Then 2 mL, 5% wt of Pluronic F-108 solution was added, and 2 mins are waited. Dewetting and extrusion of TPM from the hematite were performed by pH change to ≈ 2.1, by adding (1.5 mL, 1 M) hydrochloric acid HCl. The solution was left under stirring for 3 min, and diluted four times. Polymerization was then carried out by adding (50 mg) of radical initiator azobisisobutyronitrile (AIBN) to the solution and left it under stirring for ≈ 5 min. The beaker was covered with an aluminum foil and placed in a pre-heated oven at ≈ 80 °C for 2 h. The solution was cooled down to room temperature, the excess solution above the sedimented particles was removed, and (50 mL) DI water with (1 mL, 250 mM) NaOH solution was added, giving a pH ≈ 10, and the solution was let overnight to facilitate the hydrolysis and condensation of any remaining HTS monomers. The solution was then centrifuged and rinsed multiple times to remove the excess TPM/HTS particles and the desired colloidal solution of heterodimers was obtained.

Sample Preparation: The heterodimer particles were diluted in a 6% solution of hydrogen peroxide H_2O_2 (Fisher Scientific H325-500) in DI water (Milli-Q, resistivity 18.2 MΩ cm). Samples were prepared at a low particle density of $\approx 10^{-3}$ µm^{-2}. The cell for the solution was composed of a rectangular capillary glass (VitroCom 3520-050), previously plasma cleaned (Harrick Plasma PDC-001) and thoroughly rinsed with DI water. The solution was injected into the capillary, then sealed with capillary wax (Hampton Research HR4-328). Particles sediment near the bottom

surface of the capillary, and observations with the microscope were made in this plane.

Supporting Information

Supporting Information is available from the Wiley Online Library or from the author.

Acknowledgements

Conflict of Interest

The authors declare no conflict of interest.

Data Availability Statement

The data that support the findings of this study are available from the corresponding author upon reasonable request.

Keywords

[1] A. Houdusse, *Comptes Rendus. Biol.* **2021**, *343*, 53.
[2] G. Fudenberg, M. Imakaev, C. Lu, A. Goloborodko, N. Abdennur, L. A. Mirny, *Cell Rep.* **2016**, *15*, 2038.
[3] B. Alberts, D. Bray, J. Lewis, in *Molecular Biology of the Cell*; 2nd ed., Garland, NYC **1989**.
[4] S. Li, R. Batra, D. Brown, H.-D. Chang, N. Ranganathan, C. Hoberman, D. Rus, H. Lipson, *Nature* **2019**, *567*, 1.
[5] M. Rubenstein, A. Cornejo, R. Nagpal, *Science* **2014**, *345*, 795.
[6] Z. Ye, Y. Wang, S. Liu, D. Xu, W. Wang, X. Ma, *J. Am. Chem. Soc.* **2021**, *143*, 15063.
[7] H. Joh, D. E. Fan, *Adv. Mater.* **2021**, *33*, 2101965.
[8] J. F. Boudet, J. Lintuvuori, C. Lacoute, T. Barois, A. Deblais, K. Xie, S. Cassagnere, B. Tregon, D. B. Bruckner, J. C. Baret, H. Kellay, *Sci. Robot.* **2021**, *6*, eabd0272.
[9] M. He, J. P. Gales, E. Ducrot, Z. Gong, G.-R. Yi, S. Sacanna, D. J. Pine, *Nature* **2020**, *585*, 524.
[10] T. Hueckel, G. M. Hocky, S. Sacanna, *Nat. Rev. Mater.* **2021**, *6*, 1053.
[11] K. Chaudhary, Q. Chen, J. J. Juarez, S. Granick, J. A. Lewis, *J. Am. Chem. Soc.* **2012**, *134*, 2901.
[12] W. B. Rogers, W. M. Shih, V. N. Manoharan, *Nat. Rev. Mater.* **2016**, *1*, 16008.
[13] A. McMullen, S. Hilgenfeldt, J. Brujic, *Proc. Nat. Acad. Sci.* **2021**, *118*, 2112604118.
[14] X. Peng, M. Urso, M. Ussia, M. Pumera, *ACS Nano* **2022**, *16*, 7615.
[15] W. Wang, J. Giltinan, S. Zakharchenko, M. Sitti, *Sci. Adv.* **2017**, *3*, 1602522.
[16] B. Yigit, Y. Alapan, M. Sitti, *Adv. Sci.* **2019**, *6*, 1801837.
[17] T. O. Tasci, P. S. Herson, K. B. Neeves, D. W. M. Marr, *Nat. Commun.* **2016**, *7*, 10225.
[18] X. Liu, M. Wei, Q. Wang, Y. Tian, J. Han, H. Gu, H. Ding, Q. Chen, K. Zhou, Z. Gu, *Adv. Mater.* **2021**, *33*, 2100332.
[19] J. Palacci, S. Sacanna, A. Abramian, J. Barral, K. Hanson, A. Y. Grosberg, D. J. Pine, P. M. Chaikin, *Sci. Adv.* **2015**, *1*, 1400214.
[20] J. Katuri, W. E. Uspal, J. Simmchen, A. Miguel-Lopez, S. Sanchez, *Sci. Adv.* **2018**, *4*, eaao1755.
[21] S. Muinos-Landin, A. Fischer, V. Holubec, F. Cichos, *Sci. Robot.* **2021**, *6*, eabd9285.
[22] C. Zhou, N. J. Suematsu, Y. Peng, Q. Wang, X. Chen, Y. Gao, W. Wang, *ACS Nano* **2020**, *14*, 5360.
[23] L. Huang, J. L. Moran, W. Wang, *JCIS Open* **2021**, *2*, 100006.
[24] A. Gao, R. R. Murphy, W. Chen, G. Dagnino, P. Fischer, M. G. Gutierrez, D. Kundrat, B. J. Nelson, N. Shamsudhin, H. Su, J. Xia, A. Zemmar, D. Zhang, C. Wang, G.-Z. Yang, *Sci. Robot.* **2021**, *6*, eabf1462.
[25] C. K. Schmidt, M. Medina-Sanchez, R. J. Edmondson, O. G. Schmidt, *Nat. Commun.* **2020**, *11*, 5618.
[26] J. Wang, R. Dong, H. Wu, Y. Cai, B. Ren, *Nano-Micro Lett.* **2020**, *12*, 11.
[27] Z. Wu, J. Troll, H.-H. Jeong, Q. Wei, M. Stang, F. Ziemssen, Z. Wang, M. Dong, S. Schnichels, T. Qiu, P. Fischer, *Sci. Adv.* **2018**, *4*, eaat4388.
[28] Y. Alapan, U. Bozuyuk, P. Erkoc, A. C. Karacakol, M. Sitti, *Sci. Robot.* **2020**, *5*, eaba5726.
[29] A. C. Hortelao, C. Simo, M. Guix, S. Guallar-Garrido, E. Julian, D. Vilela, L. Rejc, P. Ramos-Cabrer, U. Cossio, V. Gomez-Vallejo, T. Patino, J. Llop, S. Sanchez, *Sci. Robot.* **2021**, *6*, 52.
[30] R. D. Leonardo, L. Angelani, D. Dell'Arciprete, G. Ruocco, V. Iebba, S. Schippa, M. P. Conte, F. Mecarini, F. D. Angelis, E. D. Fabrizio, *Proc. Natl. Acad. Sci. USA* **2010**, *107*, 9541.
[31] A. Sokolov, M. M. Apodaca, B. A. Grzybowski, I. S. Aranson, *Proc. Natl. Acad. Sci. USA* **2010**, *107*, 969.
[32] C. Maggi, J. Simmchen, F. Saglimbeni, J. Katuri, M. Dipalo, F. D. Angelis, S. Sanchez, R. D. Leonardo, *Small* **2015**, *12*, 446.
[33] S. Bianchi, G. Vizsnyiczai, S. Ferretti, C. Maggi, R. D. Leonardo, *Nat. Commun.* **2018**, *9*, 4476.
[34] S. Zhang, M. Elsayed, R. Peng, Y. Chen, Y. Zhang, J. Peng, W. Li, M. D. Chamberlain, A. Nikitina, S. Yu, X. Liu, S. L. Neale, A. R. Wheeler, *Nat. Commun.* **2021**, *12*, 5349.
[35] S. Zhang, E. Y. Scott, J. Singh, Y. Chen, Y. Zhang, M. Elsayed, M. D. Chamberlain, N. Shakiba, K. Adams, S. Yu, C. M. Morshead, P. W. Zandstra, A. R. Wheeler, *Proc. Natl. Acad. Sci. USA* **2019**, *116*, 14823.
[36] C. Maggi, F. Saglimbeni, M. Dipalo, F. D. Angelis, R. D. Leonardo, *Nat. Commun.* **2015**, *6*, 1.
[37] A. Aubret, Q. Martinet, J. Palacci, *Nat. Commun.* **2021**, *12*, 6398.
[38] D. G. Grier, *Nature* **2003**, *424*, 810.
[39] J. E. Curtis, D. G. Grier, *Phys. Rev. Lett.* **2003**, *90*, 133901.
[40] U. G. Butaite, G. M. Gibson, Y.-L. D. Ho, M. Taverne, J. M. Taylor, D. B. Phillips, *Nat. Commun.* **2019**, *10*, 1215.
[41] Y. Alapan, B. Yigit, O. Beker, A. F. Demirors, M. Sitti, *Nat. Mater.* **2019**, *18*, 1244.
[42] S. Palagi, A. G. Mark, S. Y. Reigh, K. Melde, T. Qiu, H. Zeng, C. Parmeggiani, D. Martella, A. Sanchez-Castillo, N. Kapernaum, F. Giesselmann, D. S. Wiersma, E. Lauga, P. Fischer, *Nat. Mater.* **2016**, *15*, 647.
[43] A. Aubret, M. Youssef, S. Sacanna, J. Palacci, *Nat. Phys.* **2018**, *14*, 1.
[44] A. Aubret, J. Palacci, *Soft Matter* **2018**, *14*, 9577.
[45] R. D. Leonardo, F. Ianni, G. Ruocco, *Langmuir* **2009**, *25*, 4247.
[46] F. M. Weinert, D. Braun, *Phys. Rev. Lett.* **2008**, *101*, 168301.
[47] A. Ghosh, P. Fischer, *Nano Lett.* **2009**, *9*, 2243.

**ADVANCED
SCIENCE NEWS**

www.advancedsciencenews.com

**ADVANCED
INTELLIGENT
SYSTEMS**
Open Access

www.advintellsyst.com

[48] S. Tottori, L. Zhang, F. Qiu, K. K. Krawczyk, A. Franco-Obregón, B. J. Nelson, *Adv. Mater.* **2012**, *24*, 811.

[49] D. Kagan, R. Laocharoensuk, M. Zimmerman, C. Clawson, S. Balasubramanian, D. Kang, D. Bishop, S. Sattayasamitsathit, L. Zhang, J. Wang, *Small* **2010**, *6*, 2741.

[50] L. Baraban, D. Makarov, R. Streubel, I. Mönch, D. Grimm, S. Sanchez, O. G. Schmidt, *ACS Nano* **2012**, *6*, 3383.

[51] J. Guo, J. J. Gallegos, A. R. Tom, D. Fan, *ACS Nano* **2018**, *12*, 1179.

[52] S. Du, H. Wang, C. Zhou, W. Wang, Z. Zhang, *J. Am. Chem. Soc.* **2020**, *142*, 2213.

[53] T.-Y. Huang, M. S. Sakar, A. Mao, A. J. Petruska, F. Qiu, X.-B. Chen, S. Kennedy, D. Mooney, B. J. Nelson, *Adv. Mater.* **2015**, *27*, 6644.

[54] F. Martínez-Pedrero, P. Tierno, *J. Colloid Interface Sci.* **2018**, *519*, 296.

[55] S. J. Park, S.-H. Park, S. Cho, D.-M. Kim, Y. Lee, S. Y. Ko, Y. Hong, H. E. Choy, J.-J. Min, J.-O. Park, S. Park, *Sci. Rep.* **2013**, *3*, 3394.

[56] Y. Alapan, O. Yasa, O. Schauer, J. Giltinan, A. F. Tabak, V. Sourjik, M. Sitti, *Sci. Robot.* **2018**, *3*, eaar4423.

[57] K. Xu, Y. Yang, B. Li, *Adv. Intell. Syst.* **2021**, *3*, 2100115.

[58] T. D. Nguyen, E. Jankowski, S. C. Glotzer, *ACS Nano* **2011**, *5*, 8892.

[59] G. van Anders, D. Klotsa, A. S. Karas, P. M. Dodd, S. C. Glotzer, *ACS Nano* **2015**, *9*, 9542.

[60] T. Sugimoto, K. Sakata, A. Muramatsu, *J. Colloid Interface Sci.* **1993**, *159*, 372.

[61] M. Youssef, T. Hueckel, G.-R. Yi, S. Sacanna, *Nat. Commun.* **2016**, *7*, 1.